S. Fichera, S. Ricci
Freeplay-Induced Limit-Cycle Oscillations in a T-Tail: Numerical vs Experimental Validation
Journal of Aircraft, Vol. 52, N. 2, 2015, p. 486-495
doi:10.2514/1.C032748

Freeplay-induced Limit Cycle Oscillations in a T-tail: Numerical Modeling and Experimental Validation

Sebastiano Fichera*

Sergio Ricci†

Politecnico di Milano, Dipartimento di Scienze e Tecnologie Aerospaziali, via La Masa 34, 20156 Milano, Italy

To investigate the effect of control surface freeplay, an aeroelastic wind tunnel model of a T-tail with freeplay in the control chain was developed. The T-tail rig presents a conventional vertical fin represented only by its main structural component: the main spar. No aerodynamic sectors have been used to reproduce the aerodynamic contribution of a horizontal tail. This was chosen because of the limited size of the wind tunnel chamber. Two numerical models were developed: the first one describes the dynamics of the tail by a state-space system with nonlinearity represented as a lumped element in the actuator feedback loop; and the second is described by the High Order Harmonic Balance (HOHB) approach where the response of the nonlinear system is approximated with a periodic signal.

The two approaches are then validated against experimental measurements collected during a wind tunnel testing. The results of this validation process as well the numerical and experimental approaches adopted are reported in this paper.

Keywords: freeplay, T-tail, flutter, LCO, high order harmonic balance.

Nomenclature

Δ	Fourier coefficients of the rudder rotation
δ	rudder rotation
δ_{fr}	semi-amplitude of the freeplay gap
δ_M	motor-fork assembly rotation

*Ph.D. Candidate, e-mail: fichera@aero.polimi.it, phone number: +39.02.23998310.
†Associate Professor, e-mail: sergio.ricci@polimi.it, phone number: +39.02.23998319.

q dynamic pressure, pa

$\mathbf{A}_a$, $\mathbf{B}_a$, $\mathbf{C}_a$, $\mathbf{D}_0$, $\mathbf{D}_1$, $\mathbf{D}_2$ aerodynamic state-space matrices

$\mathbf{f}_a$ vector of Generalized unsteady Aerodynamic Forces (GAFs)

$\mathbf{f}_m$ vector representing the external force

$\mathbf{H}_{am}$ generalized aerodynamic forces frequency response matrix

$\mathbf{M}_s$, $\mathbf{C}_s$, $\mathbf{K}_s$ generalized mass, damping, stiffness structural matrices

$\mathbf{q}$ structural states

$\mathbf{x_a}$ aerodynamic states

ω angular velocity of the motor shaft

Φ Fourier matrix

B motor friction torque

c reference chord, m

F Fourier coefficients of the nonlinear force

f exchanged torque/nonlinear force

i phase currents, A

J_f inertia moments of the connected fork

J_m motor moment of inertia

k reduced frequency, $\omega c/2V_\infty$

K_e rotor speed constant

K_t motor torque constant

K_δ penalty gain proportional to rotation

$K_{\dot{\delta}}$ penalty gain proportional to angular velocity

L inductance of a phase winding, H

p nondimensional Laplace variable, $sc/2V_\infty$

Q Fourier coefficients of the structural states

R resistance of a phase winding, Ω

s Lapalce variable

V_∞ asymptotic velocity, m/s

X_a Fourier coefficients of the aerodynamic states

I. Introduction

The research on nonlinear aeroelasticity and, in particular, on control surface freeplay, is motivated by the significant number of cases known in the literature of aircraft that have experienced Limit Cycle Oscillations

(LCO) caused by this phenomenon (see Dowell et al[1]). It is important to be able to accurately map the dynamics of the system under investigation to distinguish between LCO, chaotic motion and the flutter region. Although LCO is not as catastrophic to aircraft as flutter, it limits the operation regime of aircraft and may lead to structural problems, including high levels of vibrations and fatigue. Freeplay nonlinearities usually occur in control surface linkages or hinges in which the surface will not move until the magnitude of the input exceeds a certain value. In fact, freeplay in the control chains may arise as a result of many factors including wear on parts during the aircraft's life. An interesting summary of the occurrence of aeroelastic control surface LCOs caused by freeplay on Airbus aircraft is investigated by Croft.[2] A complete survey on nonlinear aeroelasticity can be found primarily in Tang and Dowell[3] and in the more recent work of Dowell et al.[4]

Woolston et al.[5] investigated nonlinearities in structural stiffness and control surface linkages. They created several models with freeplay, hysteresis, cubic-hardening and cubic-softening nonlinearities in the torsion mode. For general wing motion, they observed that the flutter velocity decreased as the initial disturbance increased and that the stability of the system was highly dependent on the magnitude of the initial condition. They also noted that a cubic-hardening nonlinearity caused LCOs above the open-loop flutter velocity and that a cubic-softening spring caused LCOs at airspeeds below the linear flutter velocity.

Tang and Dowell[6] introduced a freeplay nonlinearity in the torsion stiffness of the flap of a 3 *dof* airfoil and examined the nonlinear aeroelastic response. For various initial conditions, they created maps of the system response to describe the location of periodic limit cycles, chaotic motion, and divergent motion. They concluded that limit cycle motion is dependent on the freestream velocity, initial pitch condition, magnitude of the freeplay nonlinearity and initial conditions.

To investigate LCO phenomena in more depth from the viewpoint of efficient numerical modeling and a possible active control implementation, a numerical-experimental research activity started at the Department of Aerospace Science and Technology of Politecnico di Milano three years ago where a dedicated wind tunnel model of a T-tail equipped with a rudder and control system was designed, manufactured and tested. This study summarizes the results of this research and is organized as follows: section II describes the details of the wind tunnel model and control chain especially designed for this research; sections III and IV describe the finite element model and the development of state-space aeroservoelastic system, respectively; sections V and VI describe the two numerical approaches adopted here to model the LCO (i.e., the Nonlinear Time Marching Model and the High Order Harmonic Balance approximation (HOHB)); section VII reports a comparison between the numerical and experimental results, while section VIII draws the conclusions of the study.

II. T-tail Experimental Model

The T-tail unit considered in this study, depicted in Figure 2, is one of the so-called X-DIA, a 1 : 10 aeroelastic wind tunnel model representative of a non-conventional three-surface regional jet (called the Target Aircraft), which has been intensively investigated in the last few years at the Department of Aerospace Science and Technology, Politecnico di Milano DAST-POLIMI (see[7,8,9]). The rudder was chosen because it is expected to be an aerodynamic surface that operates for a large portion of its life with null loading, a condition where the effects of freeplay may become more evident. The basic elements of the rudder control chain are shown in the block scheme in Figure 1. Two different angular position sensors are included, one upstream and one downstream of the freeplay; both investigate the actual system response and compute the error with respect to the required angular position.

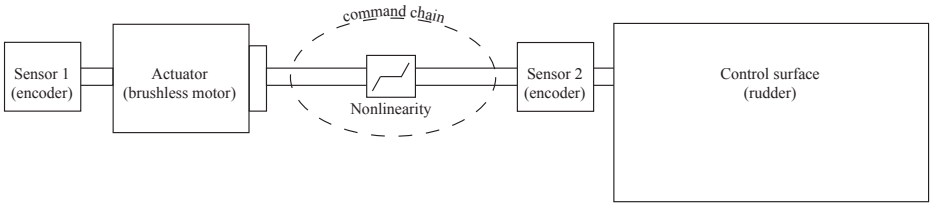

Figure 1: Control chain

The T-tail experimental model was built to scale to keep the same Froude number of the Target Aircraft (i.e., the reference regional aircraft considered during the initial aircraft design). The elements that compose the wind tunnel model are shown in Figure 2. The core is composed of dynamically-scaled spars, which are inserted in a series of sectors made of Styrofoam covered by carbon fiber skins. The fin structure is made of an aluminum alloy beam that is covered by five aerodynamic sectors that are used to define the airfoil shape. Table 1 summarizes the geometric characteristics of the T-tail. The experiments of this study were conducted at the Politecnico di Milano in the low-speed closed-return wind tunnel of the Aerodynamics Laboratory in the Aerospace Science and Technology Department (PSWT). The wind tunnel has a rectangular test section 1.5 m by 1 m, a maximum wind velocity of 55 m/s and a freestream turbulence level of less than 0.1%.

Because the size of the test chamber is limited, and the contribution of the horizontal tail to the freeplay LCO is expected to be low, the horizontal tail plane considered in the preliminary design was reduced to keep the same dynamic contribution but neglect the aerodynamic one. Consequently, the aluminum alloy spars of the horizontal tail were not covered by the aerodynamic sectors, and ballast had to be added to obtain the correct inertial properties (see Figure 2a). This is typical for these types of experiments when a complete model will not fit into the wind tunnel, see.[10,11] The span of the horizontal tail was set to 2/3 of the test section width.

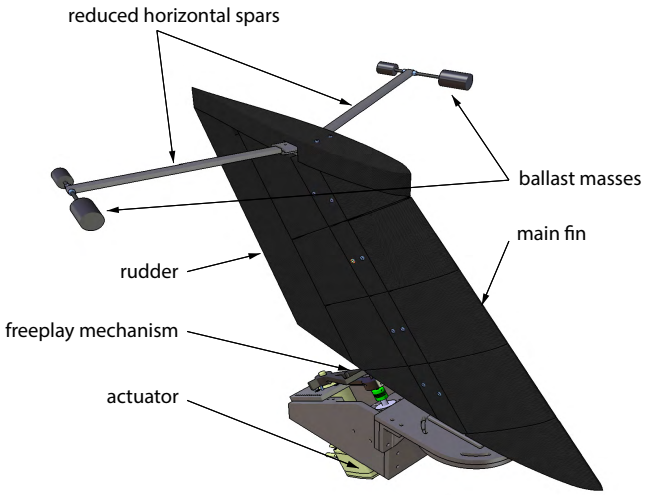

(a) Model rendering

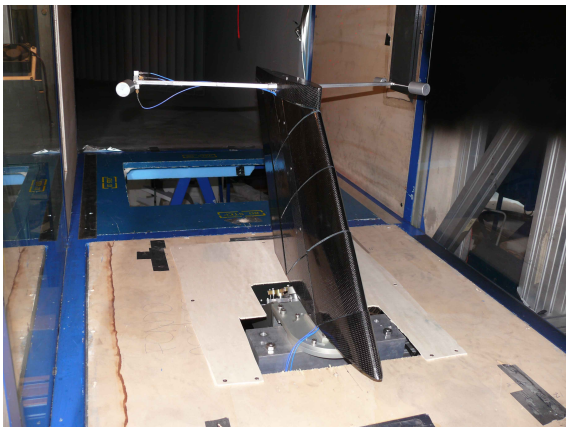

(b) Model in the wind tunnel

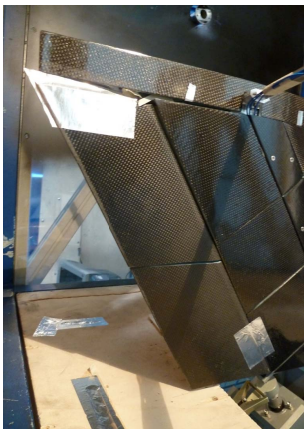

(c) Half rudder

Figure 2: T-tail aeroelastically scaled wind tunnel model.

To have a variable amplitude freeplay, the mechanism shown in Figure 3 was introduced into the control chain between the actuator and the rudder. This mechanism is composed of a rigid linkage connected to the rudder that ends with a pin that is slipped into a fork connected to the gear of the electric motor that is used to actuate the control surface. The connecting fork mechanism allows the behavior of the control surface to range from having no freeplay up to ±10 degrees by changing the position of the electric motor with respect to the rudder hinge axis, the hole where the pin is screwed and, at last, the shape of the fork. This design solution allows an increase in the amount of freeplay gap with a resolution of 0.5 degs. The angular position of the motor-fork assembly is defined by a PID controller using an angular encoder embedded into the motor for feedback. The rudder surface was cut in the middle along the span, the portion near the root was fixed to the main fin and the tip was left moveable, as shown in Figure 2c. This design was chosen because it increases the unsteady nature of the rudder.

A. Measurements, Data Acquisition and Control

The rotation of the rudder is measured by an incremental encoder connected to the rudder hinge axis at the fin root. A second encoder is used to measure the rotation of the motor-fork assembly. Three uniaxial accelerometers were placed at the center, at the leading and at the trailing edge of the fin tip. A triaxial accelerometer was also placed at the tip of the reduced horizontal tail plane. All data acquisition and system control was implemented using the RealTime Application Interface (RTAI),[12] an open-source real-time operating system developed at Politecnico di Milano.

Table 1: T-tail specifications.

Characteristic	Notation	Units	Fin
Airfoil			NACA 0015
Span	b	m	0.405
Area	S	m^2	0.212
Root Chord	C_r	m	0.593
Tip Chord	C_e	m	0.452
Mean Aerodynamic Chord	cma	m	0.526
Aspect Ratio	λ		0.774
Sweep Angle	Λ	deg	36.750
Taper	r		0.762
Rudder Root Chord	C_{r_t}	m	0.165
Rudder Tip Chord	C_{e_t}	m	0.125

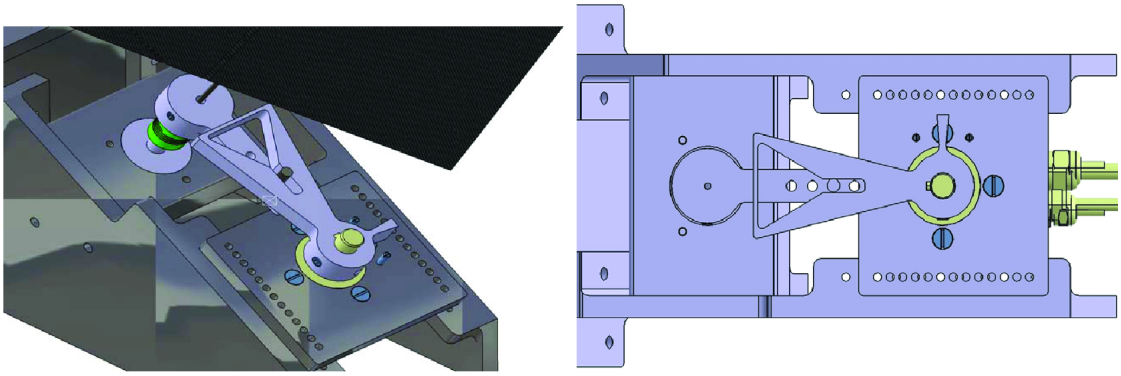

Figure 3: Kinematic chain designed in order to achive a variable amplitude freeplay system.

III. Finite Element Model

The bases for the numerical models developed hereafter are the structural Finite Element (FE) model and the aerodynamic Doublet Lattice Model (DLM) in MSC.Nastran. A preliminary modal test on the experimental model was used to identify the natural frequencies of the system and to update the numerical model accordingly. The cross MAC matrix in Figure 4a, shows a high level of correlation (higher than .85) for the first six modes, except for the third one that does not find a corresponding numerical value. The comparison of the first numerical with the experimental mode shapes is depicted in Figure 4b. Table 2 shows a comparison between the numerical and experimental natural frequencies; an error near 0.2% for the first four modes is found but increases up to 15% for the fifth.

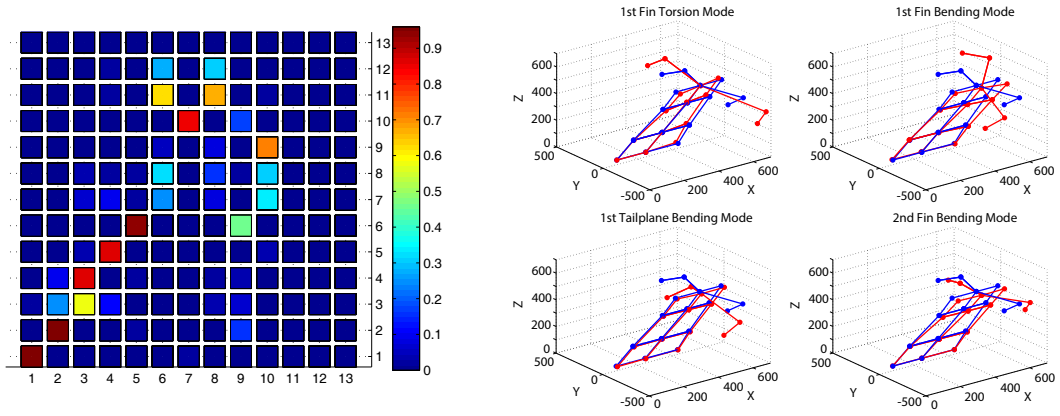

(a) Cross MAC numerical-experimental model

(b) Mode Shapes

Figure 4: MAC and Mode Shapes.

Table 2: T-tail Frequencies and Mode shapes.

Numerical model		Experimental model	
Mode Shape	Frequency [Hz]	Mode Shape	Frequency [Hz]
1 - 1^{st} Fin Torsion Mode	9.36	1 - 1^{st} Fin Torsion Mode	9.37
2 - 1^{st} Fin Bending Mode	11.63	2 - 1^{st} Fin Bending Mode	11.61
-	-	3 - 1^{st} Ballast Dummy Mode	12.42
3 - 1^{st} Tailplane Bending Mode	13.07	4 - 1^{st} Tailplane Bending Mode	13.08
4 - 1^{st} Tailplane In-Plane Mode	18.18	5 - 1^{st} Tailplane In-Plane Mode	18.17
5 - 2^{nd} Fin Bending Mode	23.22	6 - 2^{nd} Fin Bending Mode	19.90
-	-	7 - 2^{nd} Ballast Dummy Mode	28.64
-	-	8 - 3^{rd} Ballast Dummy Mode	30.94
-	-	9 - 4^{rd} Ballast Dummy Mode	36.39
6 - 1^{st} Fin In-Plane Mode	36.80	-	-
7 - 1^{st} Tailplane Torsion Mode	38.45	10 - 1^{st} Tailplane Torsion Mode	38.42

IV. State-Space Aeroelastic System

The aeroelastic system is described in Eq. 1:

$$\mathbf{M}_s\ddot{\mathbf{q}} + \mathbf{C}_s\dot{\mathbf{q}} + \mathbf{K}_s\mathbf{q} = q\mathbf{f}_a + \mathbf{f}_m \tag{1}$$

where $\mathbf{M}_s$, $\mathbf{C}_s$ and $\mathbf{K}_s$ are the mass, damping and stiffness structural matrices, respectively; $\mathbf{f}_a$ is the vector of Generalized unsteady Aerodynamic Forces (GAFs); and $\mathbf{f}_m$ represents the external force. The dimension of the generalized model that indicates the number of modes retained is m. The GAFs are computed in the reduced-frequency k domain by using the classical Doublet Lattice Method (DLM), which is:

$$\mathbf{f}_a = \mathbf{H}_{am}(k, M_\infty)\mathbf{q}. \tag{2}$$

The model of Eq. 2 can be fitted into a state-space system by using the classical Roger's expansion,[13] where m_a is the number of reduced aerodynamic modes

$$\mathbf{H}_{am}(p) \simeq \mathbf{D}_0 + \mathbf{D}_1 p + \mathbf{D}_2 p^2 + \sum_{i=1}^{N} \frac{p}{p - \beta_i}\mathbf{E}_i \tag{3}$$

and $p = \frac{sc}{2V_\infty}$ is the non-dimensional Laplace variable. This expression can be easily transformed into a classical state-space time-domain system:

$$
\begin{aligned}
(\frac{c}{2V_\infty})\dot{\mathbf{x}}_a &= \mathbf{A}_a\mathbf{x}_a + \mathbf{B}_a\mathbf{q} \\
\mathbf{f}_a &= \mathbf{C}_a\mathbf{x}_a + \mathbf{D}_0\mathbf{q} + (\frac{c}{2V_\infty})\mathbf{D}_1\dot{\mathbf{q}} + (\frac{c}{2V_\infty})^2\mathbf{D}_2\ddot{\mathbf{q}}
\end{aligned}
\tag{4}
$$

and finally the aeroelastic system can be rewritten in the following form:

$$
\begin{bmatrix} \mathbf{I} & \mathbf{0} & \mathbf{0} \\ \mathbf{0} & (\mathbf{M}_s - q(\frac{c}{2V_\infty})^2\mathbf{D}_2) & \mathbf{0} \\ \mathbf{0} & \mathbf{0} & \mathbf{I} \end{bmatrix} \begin{Bmatrix} \dot{\mathbf{q}} \\ \ddot{\mathbf{q}} \\ \dot{\mathbf{x}_a} \end{Bmatrix} = \begin{bmatrix} \mathbf{0} & \mathbf{I} & \mathbf{0} \\ -(\mathbf{K}_s - q\mathbf{D}_0) & -(\mathbf{C}_s - q(\frac{c}{2V_\infty})\mathbf{D}_1) & q\mathbf{C}_a \\ (\frac{2V_\infty}{c})\mathbf{B}_a & \mathbf{0} & (\frac{2V_\infty}{c})\mathbf{A}_a \end{bmatrix} \begin{Bmatrix} \mathbf{q} \\ \dot{\mathbf{q}} \\ \mathbf{x}_a \end{Bmatrix} + \begin{bmatrix} \mathbf{0} \\ \mathbf{B}_s \\ \mathbf{0} \end{bmatrix} \left\{ \mathbf{f}_m \right\}. \tag{5}
$$

The procedure described above is implemented using the in-house software MASST[14] that is able to generate a Reduced Order Model (ROM) in the time domain after it is supplied with the structural and aerodynamic matrices for the reduced frequency, as calculated with MSC.Nastran. The resulting ROM used for the development of the numerical model hereafter is composed of a rigid mode, the rudder control mode and additional 9 elastic modes ($m = 10$); these modes consist of the first and second fin torsion and bending modes, the first tailplane bending mode, the in-plane and torsion modes, the first and last fin in-plane mode, and the first ballast mode. These modes were chosen to yield a representative basis of the aeroelastic model in the frequency range of interest.

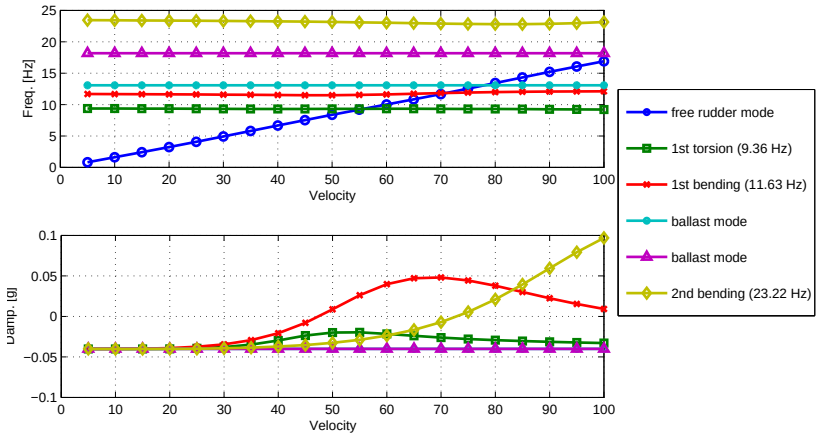

Figure 5: V-g V-f diagrams.

The aeroelastic behavior of the model is shown in the numerical $V-g$-$V-f$ flutter diagrams computed with the free surface (see Figure 5). The first (11.63 Hz) and the second ($23.22Hz$) fin bending modes cross the zero damping line, respectively, at $47m/s$ and $78m/s$.

V. Nonlinear Time Marching Approach

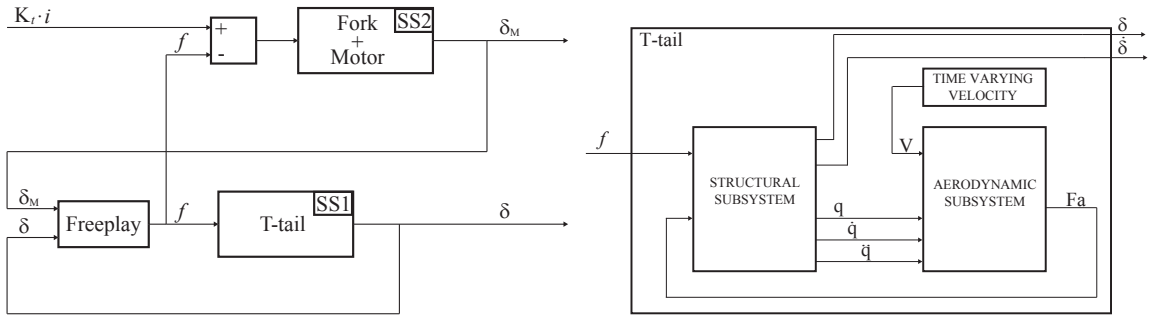

(a) Sub-systems block scheme

(b) Enlargement of T-tail sub-system (SS1)

Figure 6: Systems block scheme.

Figure 6 shows the block schemes of the nonlinear time-marching model. Two sub-systems were designed: the first one describes the aeroelastic model of the T-tail using the state-space model described in Eq. 5, while the second one describes the dynamic behavior of the actuator. Because the experimental tests showed a hysteretic behavior when decreasing the airstream speed once the LCO is established, the numerical T-tail aeroelastic system was designed to reproduce this velocity change while the simulation is running: the structural and the aerodynamic contributions were split (see Figure 6b), and the velocity was changed to an external variable of the simulation. The simulation was run until all the transient vibrations were damped, and the data recoded; then, without restarting the integration, the airstream speed is decreased, and the data were acquired again.

The second sub-system (i.e., the electro-mechanical part) is represented by Eq. 6,

$$\begin{aligned} L\frac{di}{dt} &= -Ri - K_e\omega + v \\ (J_m + J_f)\frac{d\omega}{dt} + B\omega &= K_t i - f \end{aligned} \tag{6}$$

where i is the current; v is the voltage and ω is the angular velocity of the motor axis; L and R are the motor's inductance and resistance and K_e is the rotor speed constant; J_m and J_f are the moment of inertia of the motor and the connected fork, respectively; B represents the effect of friction; and K_t is the motor

torque constant (see Table 3). The dynamics of the motor's electronics were neglected because they were too fast compared to the aeroelastic dynamics of the system. A PID system is used to control the motor current to obtain the required rudder position.

Table 3: Electro-mechanical system specifications.

Characteristic	Notation	Units	Actuator assembly
inductance of the motor	L	H	$8.2e^{-4}$
resistance of the motor	R	Ω	1.03
moment of inertia of the motor	J_m	$kg \cdot m^2$	$8.30e^{-5}$
moment of inertia of the fork	J_f	$kg \cdot m^2$	$3.0e^{-5}$
torque constant of the motor	k_t	Nm/A	$1.47e^{-1}$

When the pin is in contact with the fork, the two sub-systems are connected, and the stiffness of the movable surface is controlled by the electric motor. When the pin is separated by the fork and travels freely into the gap, the two sub-systems act as independent dynamic models. The modeling of this switching mechanism is managed using a penalty function approach[15] that computes the force exchanged between the two sub-systems as:

$$\begin{cases} f = 0 & \text{if} \quad |\delta_M - \delta| \leq \delta_{fr} \\ f = K_\delta((\delta_M - \delta_{fr}) - \delta) + K_{\dot{\delta}}(\dot{\delta}_M - \dot{\delta}) & \text{if} \quad |\delta_M - \delta| > \delta_{fr} \end{cases} \tag{7}$$

where δ_{fr} is the semi-amplitude of the gap. This approach causes a switch that represents a discrete change in the connection stiffness, as shown schematically in Figure 6. The gains K_δ and $K_{\dot{\delta}}$ are chosen following Ref.[16] to minimize both the penetration and rebound between the two sub-systems. The exchanged torque f can be considered as the nonlinear force (i.e., moment) introduced into the rudder's shaft due to the freeplay. The simulations were performed by using MATLAB Simulink with the Dormand-Prince method and a variable time step with an upper limit of 1 ms. A numerical comparison between a real PID and an infinite PID (i.e., the fork is artificially fixed into a certain position) was also investigated. The results of this analysis showed that due to the high performance of the brushless motor chosen, the effect of the controller is negligible in the frequencies and LCO amplitude ranges of interest; however, for larger amplitudes, it would have a smoothing effect on rudder motion.

VI. Numerical High Order Harmonic Balance Approximation

The aim of the Harmonic Balance (HB) method,[17,18] is to approximate the response of a given nonlinear system under LCOs with a periodic signal. Introducing high-order harmonics means that the solution is represented by a Fourier series. The procedure presented below follows the outline of Cooper *et al.*[19,20] The nonlinear aeroelastic system of Eq. 5 can be rewritten in the following general form:

$$\begin{Bmatrix} \dot{\mathbf{q}} \\ \ddot{\mathbf{q}} \end{Bmatrix} = \mathbf{A} \begin{Bmatrix} \mathbf{q} \\ \dot{\mathbf{q}} \end{Bmatrix} + \mathbf{B}\mathbf{u} \tag{8}$$

where, as previously defined, $\mathbf{q}$ is the time dependent m x 1 vector of states, and the matrices $\mathbf{A}$ and $\mathbf{B}$ represent the parameters of the nonlinear functions. The core of this approach is the approximation of the system states $\mathbf{q}$, either as a sine wave (HB) or as a Fourier series (HOHB) while it is undergoing self-excited LCOs. Eq. 9 shows the general formulation of this approach. If the order of the approximation N is equal to 1, then the scheme leads to the classical HB; otherwise, the higher-order version is produced:

$$q(t) = Q_0 + \sum_{k=1}^{N} Q_{k1}\cos(k\omega t) + Q_{k2}\sin(k\omega t) \tag{9}$$

Q_0, Q_{k1} and Q_{k2} are unknown coefficients, and ω is the fundamental frequency. Once Eq. 9 is substituted into Eq. 8, the system can be rewritten as:

$$\mathbf{g}(Q_0, Q_{k1}, Q_{k2}, \omega) = \mathbf{0} \tag{10}$$

where $\mathbf{g}$ are the m x $(2N+1)$ nonlinear algebraic equations, and ω, Q_0, Q_{k1} and Q_{k2} are the m x $(2N+1)+1$ unknowns. Due to the need to calculate the value of the fundamental frequency, the number of the unknowns is larger than that of the equations. However, the system can be solved by applying the *phase fixing* approach[19] where one of the coefficients of the series is set equal to zero (e.g., usually the first element, Q_{11}). This manipulation does not affect the generality of the solution because it only fixes the position of the wave along the period. Once the phase is fixed, Eq. 10 is solved by equating the coefficients of every sine and cosine term as well as the constant term to zero.

A. HOHB Methodology

To solve a system that undergoes self-excited oscillations, the procedure has been split into three steps with the aim of performing HOHB with lower computational cost. In the first step, the fundamental frequency is calculated, followed by the high-order unknown coefficients and finally a verification of the optimum fundamental frequency.

1. *First Step - Fundamental Frequency Calculation*

The fundamental frequency is calculated by solving the nonlinear system with an expansion order $N = 1$ with an iterative method (i.e., solving the classic first order Harmonic Balance). To decrease the number of unknowns, Q_{11} is set to zero. The unknowns are thus reduced to the number of equations (i.e. m x 3). The Fourier expansion for the structural states can be written as:

$$q^n(t) = Q_0^n + Q_{11}^n \cos(\omega t) + Q_{12}^n \sin(\omega t) \qquad n = 1, \cdots, m; \qquad Q_{11}^1 = 0; \tag{11}$$

$$\begin{Bmatrix} \mathbf{q} \\ \dot{\mathbf{q}} \\ \ddot{\mathbf{q}} \end{Bmatrix} = \begin{bmatrix} \Phi \\ \dot{\Phi} \\ \ddot{\Phi} \end{bmatrix} \Big\{ Q \Big\}. \tag{12}$$

and for the aerodynamic states is:

$$x_a^{n_a}(t) = {X_a}_0^{n_a} + {X_a}_{11}^{n_a} \cos(\omega t) + {X_a}_{12}^{n_a} \sin(\omega t) \qquad n_a = 1, \cdots, m_a; \tag{13}$$

$$\begin{Bmatrix} \mathbf{x_a} \\ \dot{\mathbf{x_a}} \end{Bmatrix} = \begin{bmatrix} \Phi \\ \dot{\Phi} \end{bmatrix} \Big\{ X_a \Big\}; \tag{14}$$

where Φ is the Fourier matrix (i.e., $\cos(\omega t)$, $\sin(\omega t)$ terms of the expansion and their derivatives). Substituting the Eqs. 12 and 14 in the Eq. 5 yields:

$$\underbrace{(\mathbf{M}_s - q(\frac{c}{2V_\infty})^2 \mathbf{D}_2)[\ddot{\Phi}]\{Q\}}_{\mathbf{M}} + \underbrace{(\mathbf{C}_s - q(\frac{c}{2V_\infty})\mathbf{D}_1)[\dot{\Phi}]\{Q\}}_{\mathbf{C}} + \underbrace{(\mathbf{K}_s - q\mathbf{D}_0)[\Phi]}_{\mathbf{K}}\{Q\} = q\mathbf{C}_a[\Phi]\{X_a\} + \mathbf{f}_m \tag{15}$$

$$\underbrace{((\frac{c}{2V_\infty})[\dot{\Phi}] - \mathbf{A}_a[\Phi])}_{\mathbf{A}}\{X_a\} = \mathbf{B}_a[\Phi]\{Q\} \tag{16}$$

$$(\mathbf{M} + \mathbf{C} + \mathbf{K})\{Q\} = \underbrace{q\mathbf{C}_a[\Phi]\mathbf{A}^{-1}\mathbf{B}_a[\Phi]}_{\mathbf{KX}}\{Q\} + \mathbf{f}_m \tag{17}$$

$$(\mathbf{M}+\mathbf{C}+\mathbf{K}-\mathbf{KX})\{Q\}=\mathbf{f}_m \tag{18}$$

Eq. 18 has m x 3 equations and the same number of unknowns, which are ω, Q_0^1, Q_{12}^1, $\ldots$, Q_0^m, Q_{11}^m, Q_{12}^m. As stated before, the system is solved using the Newton-Raphson method.

2. Second Step - High Order Unknown Coefficients Calculation

The goal of the first step is to obtain the fundamental frequency necessary to solve the system (Eq. 18), as a linear system with only Q_0^n, Q_{k1}^n, Q_{k2}^n, $k=1,\cdots,N$ and $n=1,\cdots,m$ as unknowns. The complete Fourier expansion for the structural states is:

$$q^n(t)=Q_0^n+\sum_{k=1}^{N}Q_{k1}^n\cos(k\omega t)+Q_{k2}^n\sin(k\omega t)\qquad k=1,\cdots,N;\qquad n=1,\cdots,m; \tag{19}$$

and for the aerodynamic states:

$$x_a^{n_a}(t)={X_a}_0^{n_a}+{X_a}_{k1}^{n_a}\cos(\omega t)+{X_a}_{k2}^{n_a}\sin(\omega t)\qquad k=1,\cdots,N;\qquad n_a=1,\cdots,m_a; \tag{20}$$

The Fourier matrices have the same structure as the ones in Eq. 12 and Eq. 14, but their size is now m x $(2N+1)$. Eq. 22 is the final form of the equation for the HOHB approach:

$$\underbrace{(\mathbf{M}+\mathbf{C}+\mathbf{K}-\mathbf{KX})}_{\mathbf{Z}}\{Q\}=\mathbf{f}_m \tag{21}$$

$$\{Q\}=\mathbf{Z}^{-1}\mathbf{f}_m. \tag{22}$$

The Fourier coefficients of the nonlinear function were evaluated using the Discrete Fourier Transform (DFT). Solve the system numerically, the constant terms and the cosine and sine coefficients are equated to zero. For this reason, the Fourier matrices $[\Phi]$, $[\dot{\Phi}]$, $[\ddot{\Phi}]$, etc., which are of dimension $(m, m(2N+1))$, are expanded to have dimension $(m(2N+1), m(2N+1))$. The system matrices are also expanded by spreading the elements along the diagonal to match the dimension of the HO model and allowing a solution.

3. Nonlinear Force

One of the main issues of the HOHB is the representation of the nonlinear force $\mathbf{f}_m$. The idea is to describe this function as a Fourier series:

$$f(t)=F_0+\sum_{k=1}^{N}F_{k1}\cos(k\omega t)+F_{k2}\sin(k\omega t) \tag{23}$$

and to use the same procedure as before to obtain the Fourier matrix:

$$f(t) = [\Phi]\{F\}; \tag{24}$$

The force is properly introduced in the aeroelastic system by the matrix $\mathbf{B}_s$, which spreads the nodal force on the modal *dof*, as shown in Eq. 25:

$$\mathbf{f}_m = \mathbf{B}_s f \tag{25}$$

$$\mathbf{f}_m = \mathbf{B}_s[\Phi]\{F\} \tag{26}$$

Substituting Eq. 26 in Eq. 22, the whole HOHB system is built as:

$$\{Q\} = \mathbf{Z}^{-1}\mathbf{B}_s[\Phi]\{F\}. \tag{27}$$

The nonlinear force is a consequence, in this case, of the freeplay motion δ of the control surface. For this reason, it is necessary to define the correlation between δ and f.

As in the equations above, the displacement δ has been expanded by a Fourier series:

$$\delta(t) = \Delta_0 + \sum_{k=1}^{N} \Delta_{k1}\cos(k\omega t) + \Delta_{k2}\sin(k\omega t) \tag{28}$$

$$\delta(t) = [\Phi]\{\Delta\} \tag{29}$$

The relation between the rudder motion and the force is represented by Eq. 30:

$$\begin{cases} f = -K_\delta|\delta - \delta_{fr}| & \text{if} \quad \delta < -\delta_{fr} \\ f = 0 & \text{if} \quad -\delta_{fr} \leq \delta \leq \delta_{fr} \\ f = K_\delta|\delta - \delta_{fr}| & \text{if} \quad \delta > \delta_{fr} \end{cases} \tag{30}$$

and is shown in Figure 7.

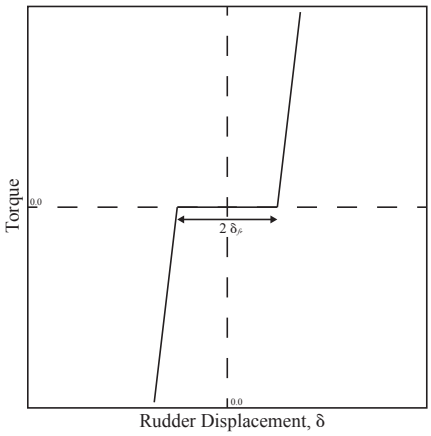

Figure 7: Freeplay stiffness.

4. Step three - Optimum Fundamental Frequency Verification

The inner HOHB procedure can be summarized in the following steps:

1. Choose the airspeed and the initial guess signal δ and ω and then calculate the coefficients Δ_0, Δ_{11} and Δ_{12};
2. Calculate the guess force and the coefficients F_0, F_{11} and F_{12}, evaluating the guess signal with the associated nonlinear function;
3. Solve Eq. 18 to obtain the fundamental frequency ω_f;
4. Choose an initial guess signal δ znd ω_f and calculate the coefficients Δ_0, Δ_{k1} and Δ_{k2});
5. Calculate the guess force and the coefficients F_0, F_{k1} and F_{k2}, evaluating the guess signal with the associated nonlinear function;
6. Solve Eq. 27 to obtain the new value of δ,
7. Calculate the residual $\mathbf{R}$ as:

$$\delta_i(t) = [C_s] \begin{bmatrix} \Phi \\ \dot{\Phi} \end{bmatrix} \{Q\} \tag{31}$$

$$\mathbf{R} = \begin{bmatrix} \Delta_0^2 - \Delta_0^1 & \Delta_{11}^2 - \Delta_{11}^1 & \Delta_{22}^2 - \Delta_{22}^1 & \cdots & \Delta_{k1}^2 - \Delta_{k1}^1 & \Delta_{k2}^2 - \Delta_{k2}^1 \end{bmatrix} \tag{32}$$

8. Calculate an improved guess ($\mathbf{J}^{-1}\mathbf{R}$) using the Jacobean and iterate until the residual $\mathbf{R}$ is sufficiently small.

To verify the validity of the fundamental frequency calculated at point 3, an additional step is necessary. The value of ω_f is close to the calculated one, and the residual is evaluated. As the residual indicates an optimum point, the fundamental frequency is updated, and the inner loop is iterated.

VII. Numerical vs. Experimental Results

The two numerical approaches described in the previous sections were applied, and the results compared to the ones measured experimentally during two different wind tunnel tests. The studied configuration has a freeplay amplitude of ± 1 degs; this gap amplitude was chosen after preliminary numerical and experimental tests showed that either an increase or decrease of the amount of freeplay only scaled the amplitude of the LCO. Future investigations will examine this aspect of the problem. The initial angle of attack of the model is set to zero, and the zero position of the fork is maintained by the PID controller. The T-tail is placed in the freestream such that the control surface is resting in the middle of the freeplay region. The experimental model does not require any external excitation because small imperfections in the model start LCO motions. Transients are allowed to decay, and the rudder rotation angle and the accelerometers signal are recorded. Then, the freestream speed is slowly increased to a new value, and the process is repeated. The maximum freestream speed explored was 50 m/s due to the maximum PSWT speed. Two runs were performed, increasing and decreasing the wind tunnel speed in steps of 1 m/s, respectively.

An approach similar to the one adopted for the experimental tests was used for the time-integrated model; however, in this case, the excitation is generated by an impulsive rotation of the rudder. The freestream speed explored ranges from 10 m/s to 100 m/s with an increasing step of 5 m/s that is reduced to 1 m/s near the switching point.

The procedure presented in section 4 was implemented on the same model. For this study, an order of approximation $N = 15$ was chosen to be able to observe the significant superharmonics shown in the experimental tests.

The following figures show the LCO amplitude and frequency (Figure 8), waveforms and portraits diagrams (Figures 9 and 10), and FFTs (Figures 11 and 13) at different speeds (50, 75 and 85 m/s). The numerical results, which were obtained by a direct time-marching integration of the nonlinear model and by the HOHB method, show two LCO regions, identified by the red-bulleted line in Figure 8). The first region is determined by the flutter of the first bending mode, while the second is a combination of the first and second mode flutters. Conversely, the experimental tests were able to show only the low frequency LCO region, which is identified by the black-triangle line in Figure 8; this was due to the limited velocity range of the PSWT. A closer look at Figure 8a shows that the average amplitude percentage error between the time-integrated results and the experimental data are near 4%; the HOHB tended to underestimate the

experimental values in the same range at nearly 10%. The frequency vs. velocity diagram of Figure 8b shows that the fundamental LCO frequency is well predicted by both numerical methods and that it has an average error with the experimental data of less than 2%.

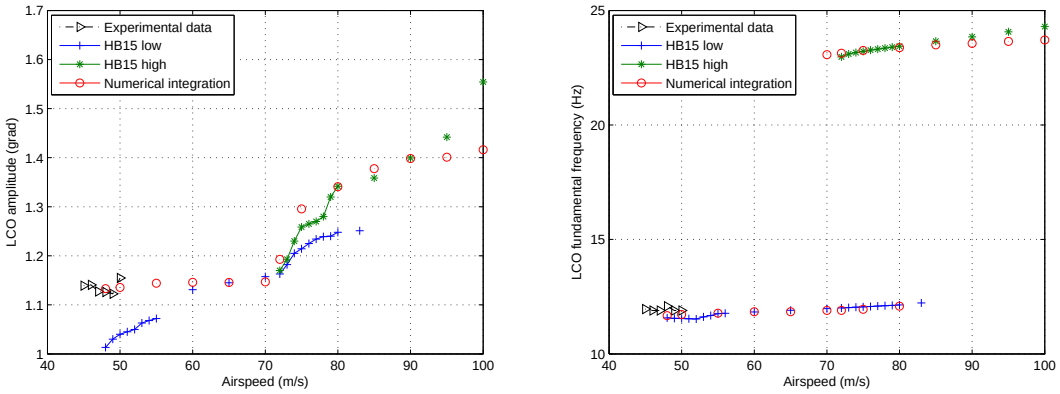

(a) Amplitude - Velocity

(b) Frequency - Velocity

Figure 8: Experimental, Numerical Integration and HOHB comparison

Figure 9 shows the amplitude of the rudder angular rotation and its velocity for a single period as a waveform comparison (Figure 9a) and portrait diagram (Figure 9b). As stated before, the maximum LCO amplitude error is near 4% while the maximum velocity is numerically underestimated at 60%. Additionally, in the experimental model, the contact point between the rudder and the freeplay boundaries occurs earlier than predicted in the numerical simulations. Moreover, the HOHB results are shown to be in good agreement with the experimental data even if the method is not completely able to catch the peaks due to the folding of freeplay stiffness (see blue and green continuous curves in Figures 9 and 10 respectively.)

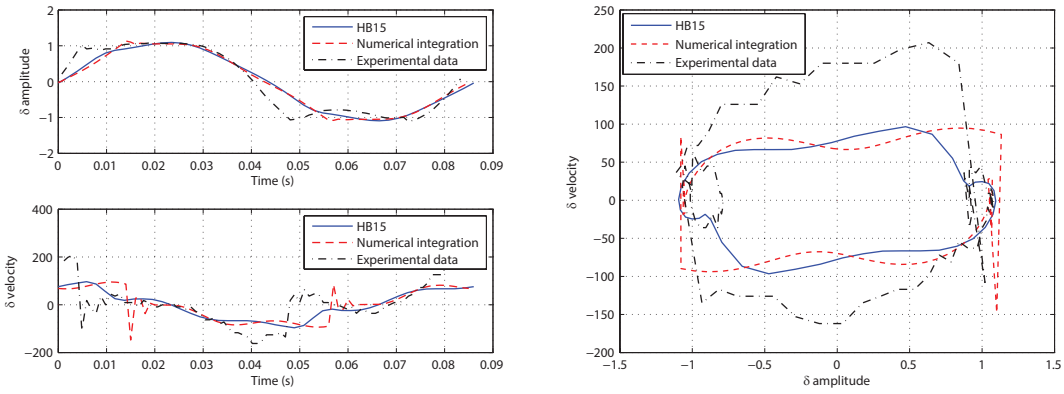

(a) one period

(b) portraits

Figure 9: Experimental, Numerical Integration and HOHB comparison at 50 m/s

Figure 10 shows the waveform and portrait comparison for the second-type LCO; however, there are no experimental data available in this case due to the higher airstream speed analyzed (i.e., $85m/s$). The trends resulting from the two methods are very similar, even if the contact region is not well predicted by the HOHB method.

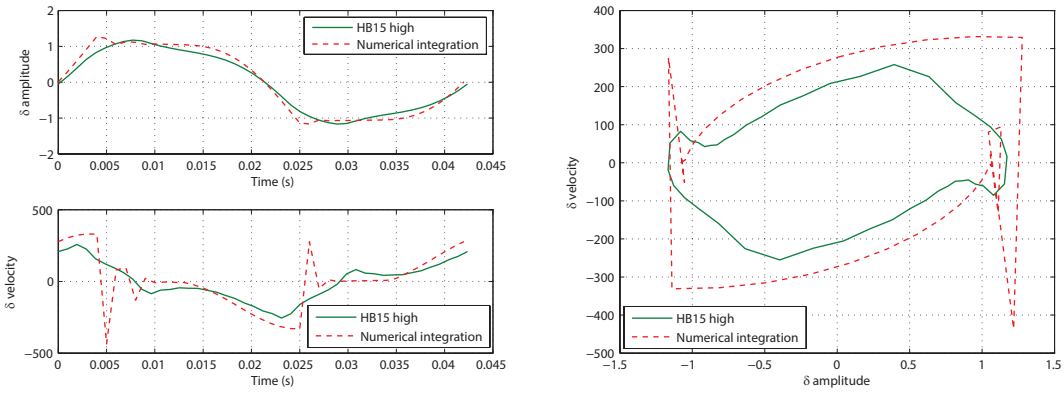

(a) one period (b) portraits

Figure 10: Numerical Integration and HOHB comparison at 85 m/s

The FFT of the rudder signal shows the characteristic path of an odd nonlinearity (see Figure 11); the basic frequency of the first banding mode is clearly visible along with its odd multiple. The FFTs in Figure 11 show a discrepancy of the second superharmonic between the experimental and numerical integration/HOHB results. This is most likely caused by an imperfect tuning of the first ballast dummy mode of the FE model with the experimental one. This difference between the two models is most likely the cause of the discrepancies highlighted by the results presented above.

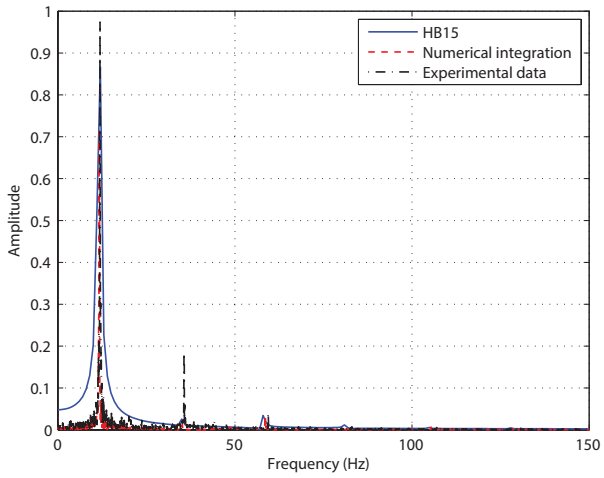

Figure 11: Experimental, Numerical Integration and HOHB FFT comparison at 50 m/s

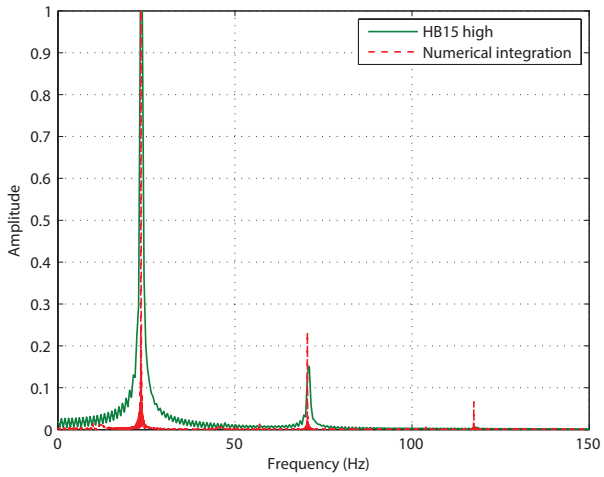

Figure 12: Numerical Integration and HOHB FFT comparison at 85 m/s

Figure 13 shows the FFT diagrams for the LCO transition region. The numerical integration results show both the frequency of the first and the second bending mode with different amplitudes; the HOHB results show different behaviors led by the guess fundamental frequency. If the guess ω is close to the low LCO, the HOHB tends to decrease to it; otherwise, it is shown that the convergence is likely: increasing the airspeed leads the HOHB only to the high LCO frequency.

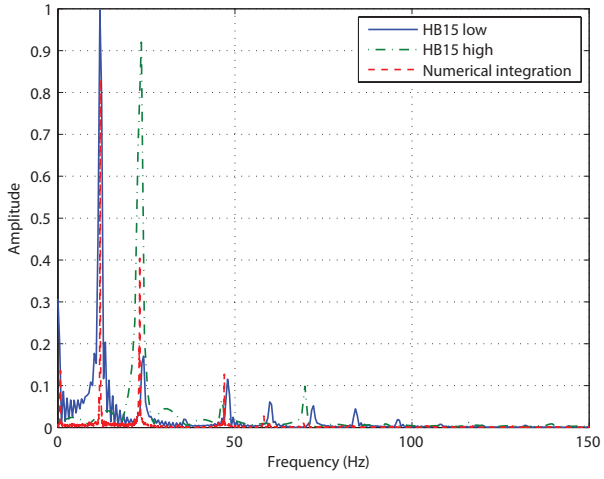

Figure 13: Numerical Integration and HOHB FFT comparison at 75 m/s

VIII. Conclusions

This paper presents an experimental-numerical investigation of limit cycle oscillations (LCO) due to the presence of freeplay on the control chain. In particular, a dedicated wind tunnel model of a T-tail equipped with a rudder driven by an electric motor where the user can easily define the freeplay value was designed, manufactured and tested. From a numerical point of view, two different approaches were implemented and tested to capture the LCO phenomenon and to correlate the results with the wind tunnel measurements (i.e., a nonlinear time-marching approach and a High Order Harmonic Balance approximation (HOHB)). While in principle both numerical approaches are able to identify the two LCOs at both low and high speeds; the experimental results available are limited to the first LCO caused by the flutter of the first bending mode; this limit was due to the maximum speed available in the wind tunnel.

The comparison between the numerical and experimental results shows generally good agreement even if the HOHB is not able to catch the vibration peaks due to the folding of freeplay stiffness. In general, the capability of the HOHB method to capture the LCO strongly depends on the guess frequency adopted. Indeed, the first LCO is identified only in the case of a guess frequency close to it; otherwise, the HOHB method tends to identify the higher LCO.

The work presented here serves as a verification and foundation for the next stage of this project, which is focused on the design of a dedicated control system that is able to reduce the LCO to be tested and validated during a new wind tunnel test campaign.

Acknowledgments

The authors would like to thank Paolo Mantegazza and Giuseppe Quaranta for their generous advice, and Alessandro Scotti for his support during the experimental model construction.

References

[1]Dowell, E. H., Edwards, J., and Strganac, T., "Nonlinear Aeroelasticity," *Journal of Aircraft*, Vol. 40, No. 5, 2003, pp. 857–874.

[2]Croft, J., "Airbus Elevator Flutter: annoying or dangerous?" *Aviation Week and Space Technology*, Vol. 155, No. 9, August 2001, pp. 41.

[3]Dowell, E. H. and Tang, D., "Nonlinear Aeroelasticity and Unsteady Aerodynamics," *AIAA Journal*, Vol. 40, No. 9, 2002, pp. 1697–1707.

[4]Dowell, E. H., "Some recent advances in nonlinear aeroelasticity: fluid-structure Interaction in the 21st Century," *Proceedings of the* 51st *AIAA/ASME/ASCE/AHS/ASC Structures, Structural Dynamics, and Materials Conference*, Orlando, FL, 12–15 April 2010.

[5]Woolstone, D., Runyan, H., and Andrews, R., "An Investigation of Effects of Certain Type of Structural Nonlinearities

on Wing and Control Surface Flutter," *Journal of Aeronautical Sciences*, Vol. 24, 1957, pp. 57–63.

[6]Tang, D. M. and Dowell, E. H., "Flutter and Stall Response of a Helicopter Blade with Structural Nonlinearity," *Journal of Aircraft*, Vol. 29, No. 5, 1992, pp. 953–960.

[7]Ricci, S., Scotti, A., and Zanotti, D., "Control of an all-movable foreplane for a three surfaces aircraft wind tunnel model," *Mechanical Systems and Signal Processing*, Vol. 20, July 2006, pp. 1044–1066.

[8]Ricci, S., Scotti, A., De Gaspari, A., and Riccobene, L., "Active Aeroelastic Control over a Multisurface Wing: Modelling and Wind-Tunnel Testing," *AIAA Journal*, Vol. 47, No. 9, 2009, pp. 1995–2010, doi: 10.2514/1.34649.

[9]Mattaboni, M., Quaranta, G., and Mantegazza, P., "Active Flutter Suppression for a Three Surface Transport Aircraft by Recurrent Neural Networks," *Journal of Guidance, Control, and Dynamics*, Vol. 32, No. 4, 2009, pp. 1295–1307.

[10]Sandford, M. C., Ruhlin, C. L., and Yates, J. C. E., "Subsonic and Transonic Flutter and Flow Investigations of the T-Tail of a Large Multjet Cargo Airplane," Technical note D-4316, NASA, Langley Research Center Langley Station, Hampton, Va., February 1968.

[11]Sandford, M. C. and Ruhlin, C. L., "Experimental Parametric Studies of Transonic T-Tail Flutter," Technical note D-8066, NASA, Langley Research Center Langley Station, Hampton, Va., Decembrer 1975.

[12]Dozio, L. and Mantegazza, P., "Real Time Distributed Control Systems Using RTAI," *Sixth IEEE International Symposium on Object-Oriented Real-Time Distributed Computing (ISORC)*, Hakodate, Hokkaido, Japan, May 14–16 2003.

[13]Roger, K. L., "Airplane Math Modeling Methods for Active Control Design," Tech. Rep. CP–228, AGARD, August 1977.

[14]Masarati, P., Muscarello, V., Quaranta, G., Locatelli, A., Mangone, D., Riviello, L., and Viganò, L., "An Integrated Environment for Helicopter Aeroservoelastic Analysis: the Ground Resonance Case," *37th European Rotorcraft Forum*, Gallarate, Italy, September 13–15 2011, pp. 177.1–12.

[15]Fichera, S., *Non linearità di tipo freeplay in un modello di coda a T aeroelastico. Studio numerico e sperimentale.*, Master's thesis, Politecnico di Milano, Dipartimento di Ingegneria Aerospaziale, Milano, 2010, In italian.

[16]Hunt, K. and Crossley, F., "Coefficient of Restitution Interpreted as Damping in Vibroimpact," *Journal of Applied Mechanics*, Vol. 42, No. 2, June 1975, pp. 440–446.

[17]Kim, Y. B. and Noah, S. T., "Stability and bifurcation analysis of oscillators with piecewise-linear characteristics. A general approach," *Journal of Applied Mechanics, Transactions ASME*, Vol. 58, No. 2, 1991, pp. 545–553, Cited By (since 1996): 80.

[18]Liu, L. and Dowell, E. H., "Harmonic balance approach for an airfoil with a freeplay control surface," *AIAA Journal*, Vol. 43, No. 4, 2005, pp. 802–815, Cited By (since 1996): 25.

[19]Dimitriadis, G., Vio, G. A., and Cooper, J. E., "Application of higher-order harmonic balance to non-linear aeroelastic systems," *Collection of Technical Papers - AIAA/ASME/ASCE/AHS/ASC Structures, Structural Dynamics and Materials Conference*, Vol. 7, 2006, pp. 5176–5187.

[20]Vio, G. A., Dimitriadis, G., and Cooper, J. E., "Improved implementation of the harmonic balance method," *Collection of Technical Papers - AIAA/ASME/ASCE/AHS/ASC Structures, Structural Dynamics and Materials Conference*, Vol. 8, 2007, pp. 7879–7890.